

Determination and optimization of material parameters of particle-based LaTiO₂N photoelectrodes

Yannick K. Gaudy¹, Stefan Dilger², Steve Landsmann², Ulrich Aschauer³, Simone Pokrant⁴ and Sophia Haussener^{1,*}

¹ École Polytechnique Fédérale de Lausanne, Institute of Mechanical Engineering, Laboratory of Renewable Energy Science and Engineering, 1015 Lausanne, Switzerland

² Empa Swiss Federal Laboratories for Materials Science and Technology, Laboratory Materials for Energy Conversion, Überlandstrasse 129, 8600 Dübendorf, Switzerland

³ University of Bern, Department of Chemistry and Biochemistry, Freiestrasse 3, 3012 Bern

⁴ University of Applied Sciences Saarland, Goebenstraße 40, 66117 Saarbrücken, Germany

*Corresponding author. E-mail address: sophia.haussener@epfl.ch, tel.: +41 21 693 38 78.

Quantitative structural analysis of LTON particle-based PEs

Nominal sizes of particles were determined by using digitalized meso-structure information obtained by focused ion beam scanning electron microscopy (SEM) data. Ellipse were fitted into the individual particles and the main axis dimensions were recorded to obtain their frequency distributions¹ (Fig. S1). A log-normal distribution was fit to the three particle dimensions' frequency distribution curves.

The extracted particle orientations of LTON particle-based PEs are depicted in Fig. S2. The orientation was determined based on the vector of the longest axis of the fitted ellipse with respect to the FTO substrate's surface normal. The calculated averaged angle is 37.4° for all particles with center point within the first 1 μm of the film's thickness.

The density of LTON photoelectrodes deposited on FTO by electrophoretic deposition was determined by integrating the volumes of the different phases (Fig. S3)¹.

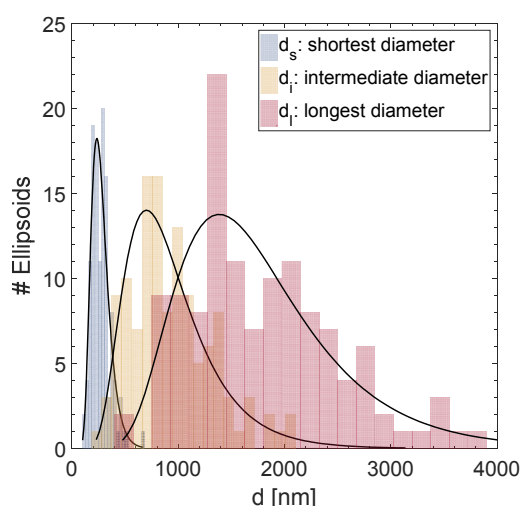


Fig. S1. Size distribution of the three ellipsoid diameters based on lognormal distributions: d_s , mean=272 nm, d_s , SD=88 nm; d_i , mean=932 nm, d_i , SD=427 nm; d_l , mean=1789 nm, d_l , SD=773 nm.

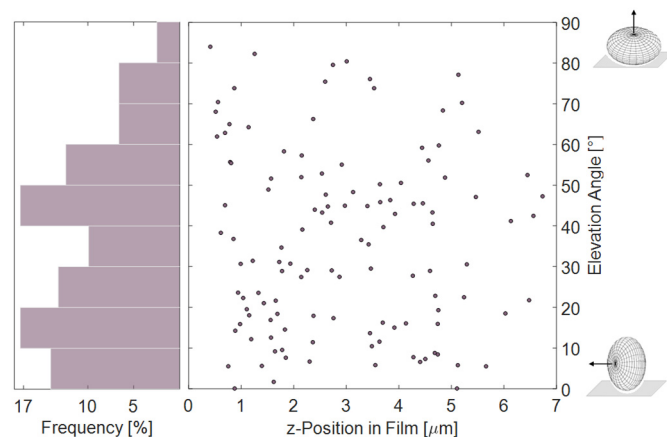


Fig. S2. Particle orientation determined by the direction of the longest diameter. Elevation angle=90°: particle lies flat relative to the FTO, and elevation angle=0°: particle stands upright relative to the FTO. The scatter plot demonstrates no trend of particle orientation as a function of z-position; however, normal vectors of the particles were elevated most frequently by 10° or 45°, as shown in the frequency distribution.

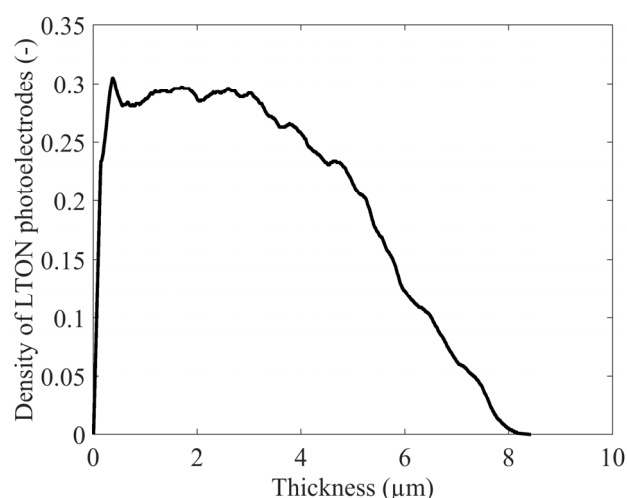


Fig. S3. Normalized density profile of LTON photoelectrodes electrophoretically deposited on a FTO substrate.

Solar simulator characteristics

The spectral irradiance of the Verasol-2 LED class AAA solar simulator from Oriel is depicted in Fig. S4. The solar simulator was calibrated using the UV-Vis spectrometer HR4000CG-UV-NIR from Ocean Optics to measure each LED's spectrum with a spectral-stepping of 0.27 nm. The total irradiance of each LED was measured with a calibrated Si diode (FDS1010 from Thorlabs).

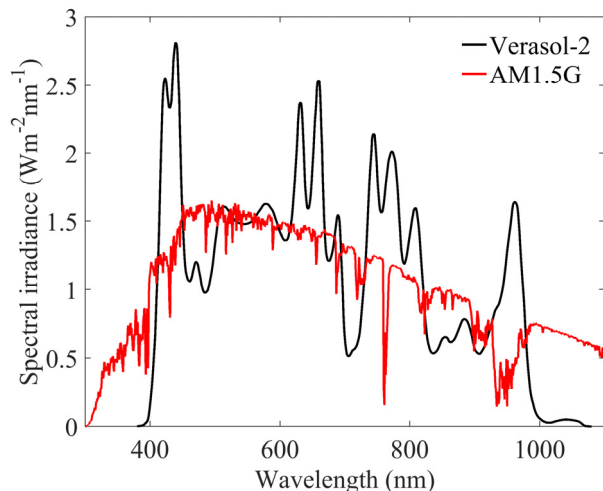


Fig. S4. Spectral irradiance of the Verasol-2 LED class AAA solar simulator from Newport and the reference spectral irradiance AM1.5G.

Open-circuit voltage

The open-circuit voltage (OCV) measurements were conducted in 0.1M Na₂SO₄ and NaOH at pH= 13.2±0.2 and under AM1.5G with a periodic light chopping every 10s. The OCV was measured after 200s of stabilization and the OCV was determined by taking the potential difference between on and off light, after the 10s transients.

We confirmed the presence of band bending at the semiconductor-electrolyte interface with OCV greater than zero (Fig. S5). The OCVs of bare-LTON PEs was smaller (0.01V under back-side illumination and 0.15V under front-side illumination) than the ones of best-LTON (0.25V under back-side illumination and 0.35V under front-side illumination). This difference was explained by less recombination at the semiconductor-electrolyte interface for best-LTON. Less recombination increased the concentration of holes at the surface and therefore the quasi-Fermi level of holes, in other words the photovoltage measured by OCV measurements.

For both types of PEs, the front-side illumination led to higher OCVs than the back-side illumination although the relative difference was smaller for best-LTON PEs (29% for best-LTON and 93% for bare-LTON). The photocurrent is fixed to zero for the OCV measurements and therefore there is no inter-particle charge transfer. In this case, the upper particles can contribute to the OCV. Upper particles are less in contact with surrounding particles. Thus, a larger surface is exposed to the semiconductor-electrolyte interface, which increases the OCV, compared to lower particles. The side of light illumination must also be considered, and since under back-side illumination most of the light is absorbed by the lower particles, the upper particles cannot contribute significantly to the OCV. In contrast, the upper particles are mostly contributing to the OCV under front-side illumination. Both effects explain the larger OCV under front-side illumination than under back-side illumination.

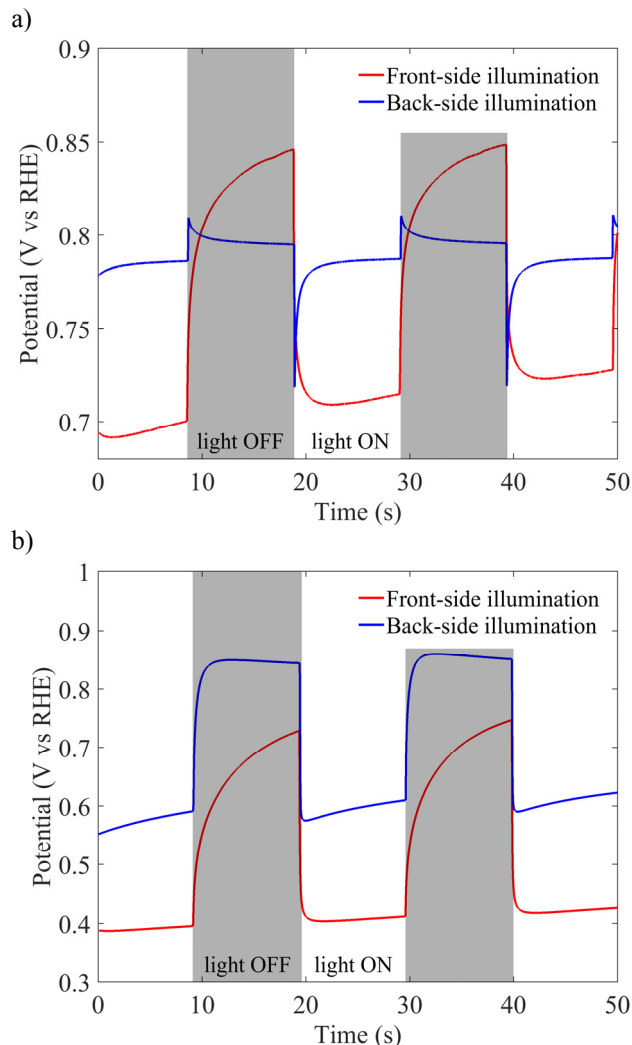


Fig. S5. Variation of the open-circuit potential under periodic light chopping of 10s for a) bare-LTON and b) best-LTON photoelectrodes immersed in 0.1M NaSO₄ and NaOH (pH=13.2) under back- (blue) and front-side (red) illumination. The OCV increased by adding a co-catalyst, i.e. the OCV of bare-LTON was 0.01V under back-side illumination while it was 0.25V for best-LTON.

Electrochemical impedance spectroscopy

The Mott-Schottky plot with frequency dispersion is depicted in Fig. S6. The experimental and simulated impedance spectra of best-LTON at 0.12V vs RHE is presented in Fig. S7.

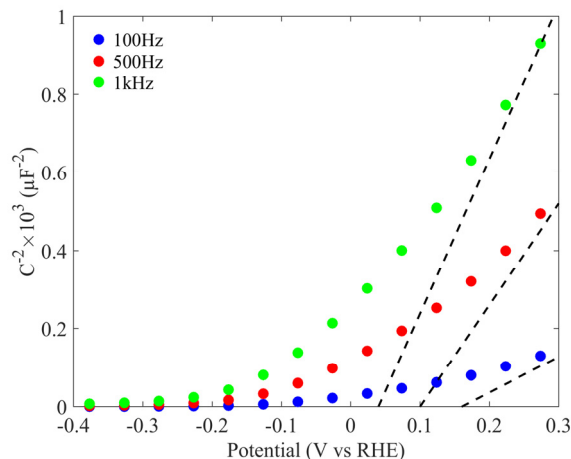


Fig. S6. Mott-Schottky plot for three frequencies (100Hz, 500Hz, 1kHz) of best-LTON electrodes immersed in 0.1M NaSO₄ and NaOH (pH=13.2) under dark conditions.

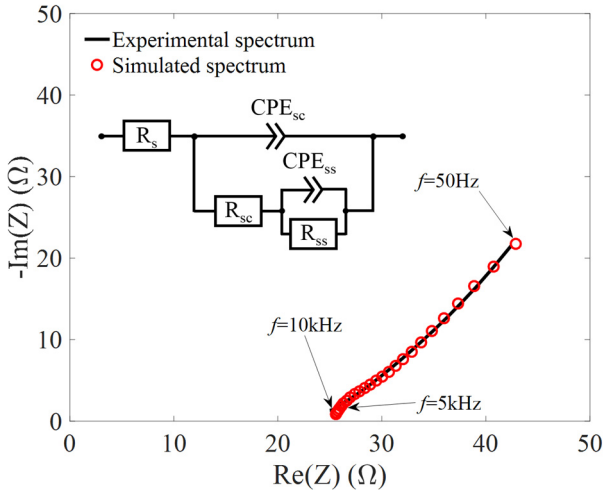


Fig. S7. Experimental and simulated impedance spectra of best-LTON photoelectrodes at 0.12V vs RHE immersed in 0.1M NaSO₄ and NaOH (pH=13.2) under dark conditions. The electrical impedances at 0.12V vs RHE are $R_s=25.43\Omega$, $R_{sc}=6.228\Omega$, $Y_{0,sc}=2.221 \cdot 10^{-5} \text{Fs}^{\alpha-1}$ with $\alpha_{sc}=0.96$, $R_{ss}=347.7\Omega$ and $Y_{0,ss}=8.182 \cdot 10^{-4} \text{Fs}^{\alpha-1}$ with $\alpha_{ss}=0.65$.

Optical parameters

The calculated Tauc plot is depicted in Fig. S8. The linear extrapolation (dashed black lines) indicates a bandgap of 1.9eV, below the well-known value of 2.1eV²⁻⁸. This underestimation of the bandgap might be due to absorption of scattered photons. If we assume a constant scattering absorption, we can remove the scattering part by shifting the zero of the y-axis in the Tauc plot (red dashed line in Fig. S8) and estimate a bandgap of 2.08eV, closer to the actual value of 2.1eV. The Kubelka-Munk (K-M) transform: $F(\rho)=(1-\rho)^2/\rho$ from total reflectance measurements (diffuse and direct) can be used to evaluate the absorbance of inhomogeneous media with light scattering such as particle-based PE. The Tauc plot based on the K-M transform of LTON particle-based PE is depicted in Fig. S9 and shows a bandgap of 2.1eV, in accordance with the known value of 2.1eV and confirming the role of light scattering in these PEs.

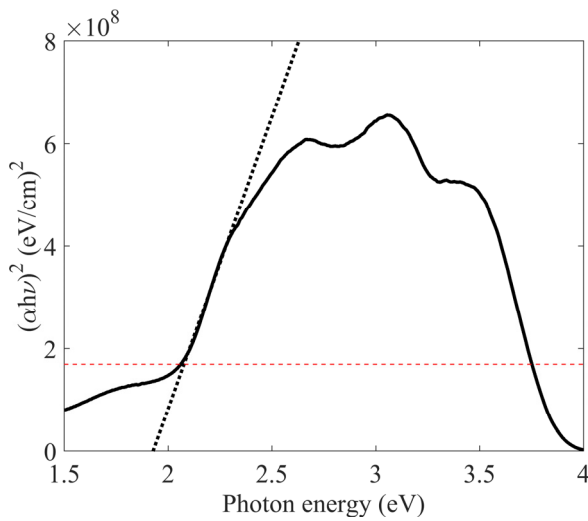


Fig. S8. Direct bandgap Tauc plot of LTON particle-based PEs based on the calculated absorption coefficient, eq. (8). The direct bandgap is found to be 1.9eV according to the linear interpolation (dashed black line). If the plot is corrected for the constant absorption of light scattering, the estimated bandgap is 2.1eV (crossing of red and black dashed lines).

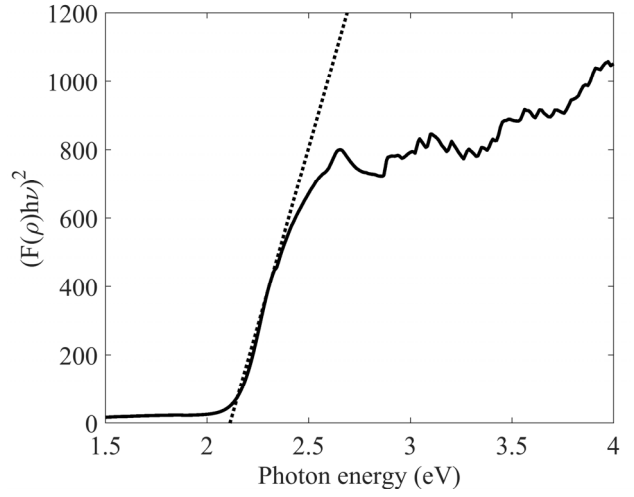


Fig. S9. Direct bandgap Tauc plot of LTON particle-based PEs based on K-M transform. The direct bandgap is found to be 2.1eV according to the linear interpolation (dashed black line).

Optical simulations

Computational details for photoabsorption model - Convergence was obtained with a direct MUMPS solver. A relative tolerance of 10^{-4} in the electric field was used as convergence criteria. Mesh convergence was obtained for linear mesh discretization with size ratio of 4, and element numbers, n_{el} , depending on the irradiation wavelength, λ , and the layer thickness, d : $n_{el} = d \cdot \beta / \lambda$ with $\beta = 200$ for SnO₂, $\beta = 150$ for LaTiO₂N, $\beta = 50$ for glass, and $\beta = 30$ for water. The number of mesh elements perpendicularly to the direction of light propagation was fixed to 5 in the domain with a width of 5μm.

Model validation by transmittance - The EMW model has the same dimension as the PEs: a slab of 2μm of air to account for reflection at the air-LTON interface, followed by 8.433μm of LTON, 360nm of SnO₂, 2.2mm of glass and again 2μm of air. Complex refractive index for bare glass (glass TCO22-15) and SnO₂ were provided by Solaronix (Fig. S10 and Fig. S11). The complex refractive index of air was taken from Ciddor⁹. The calculated transmittance under back- and front-side illumination using EMW propagation model are depicted in Fig. S12.

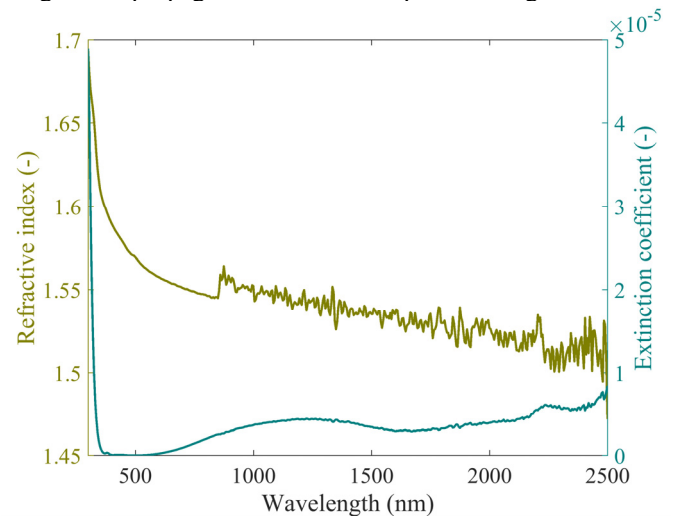


Fig. S10. Complex refractive index of bare glass of 2.2μm for TCO22-15 transparent conductive layer of Solaronix.

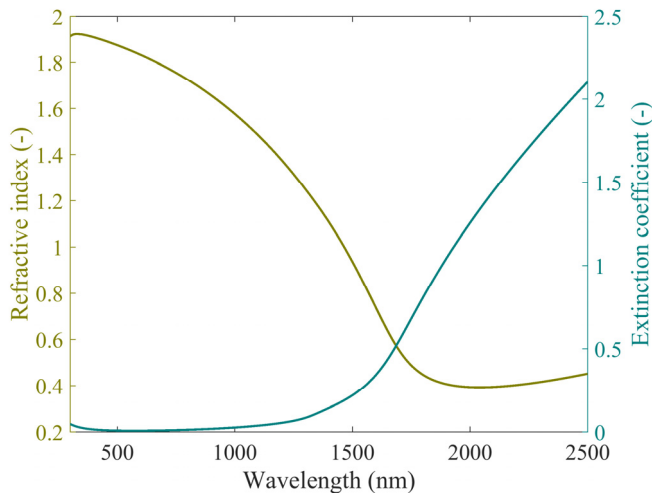


Fig. S11. Complex refractive index of SnO_2 layer of 360nm for TCO22-15 transparent conductive layer of Solaronix.

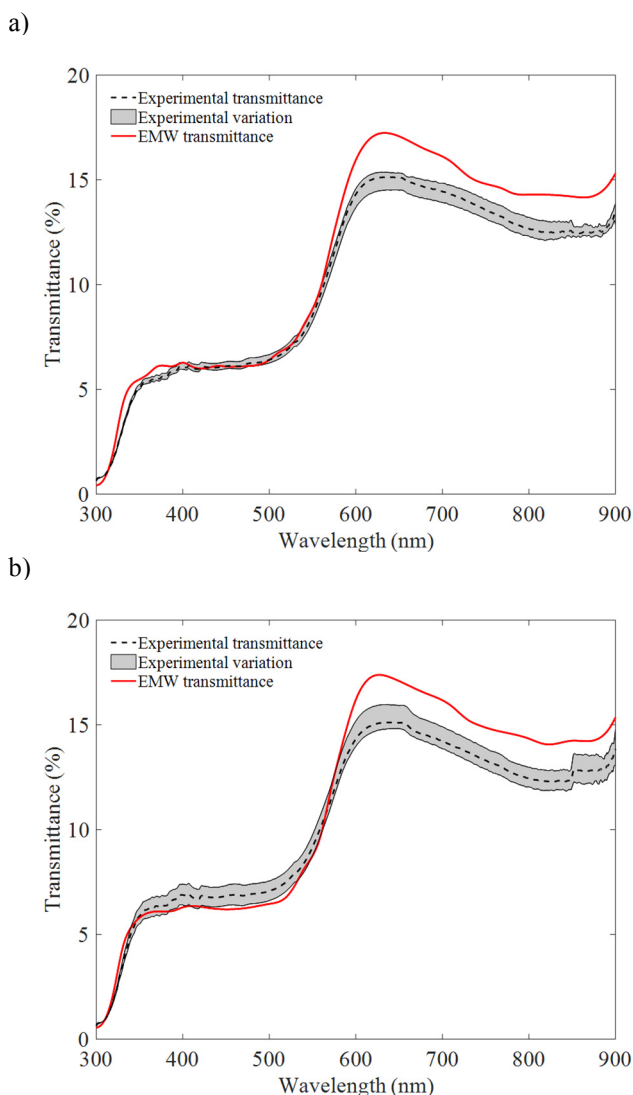


Fig. S12. Measured and calculated transmittance of LTON particle-based photoelectrode under a) back- and b) front-side illumination. Transmittance is calculated with an EMW propagation model each 10nm and a cubic spline interpolation is used for smoothing. The numerical transmittance is below 2% error compared to the measured transmittance from 400nm to 590nm (2.1eV, band gap of LTON). The experimental variation is obtained by measuring four different LTON photoelectrodes.

The calculated transmittance under back- and front-side illumination using Beer-Lambert's law are depicted in Fig. S13. The calculated transmittance for both methods is below 2% error from 400nm to 590nm, corresponding respectively to the lowest photon's wavelength emitted by the Verasol-2 solar simulator and the bandgap of LTON. The calculation of the generation rate using one of these methods would lead to a photogenerated current error of 0.005mA/cm² under front-side illumination and 0.124mA/cm² under back-side illumination, both using AM1.5G spectral irradiance. These errors are below the experimental photocurrent density variation of 0.167mA/cm² under back-side illumination and 0.204mA/cm² under front-side illumination at 1.23V vs RHE (Fig. 5).

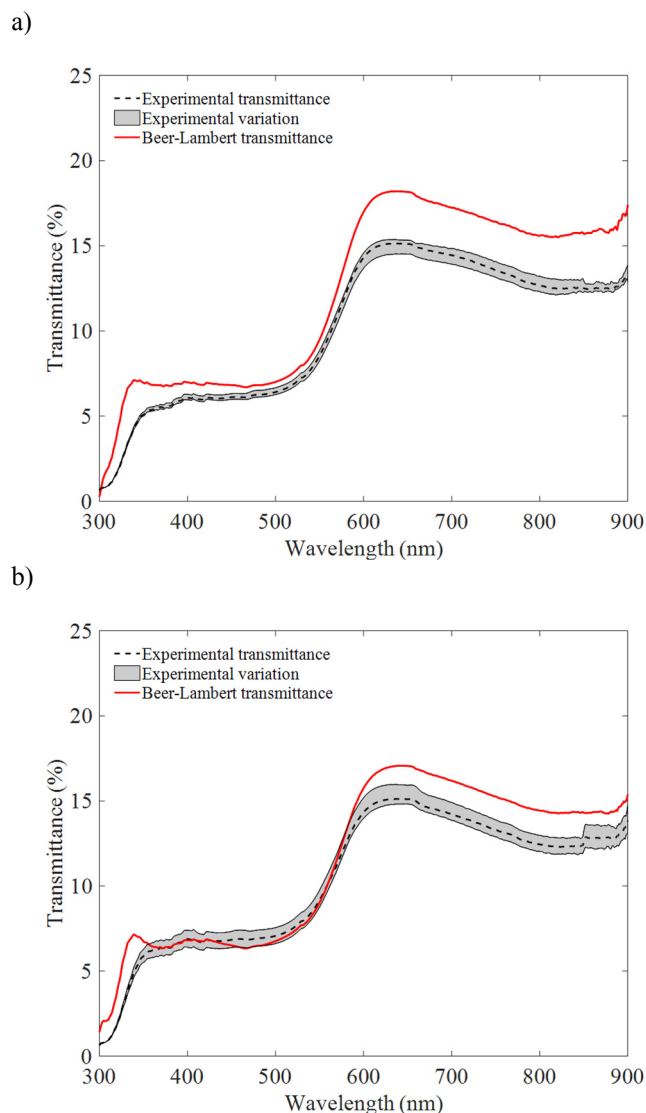


Fig. S13. Measured and calculated transmittance of LTON particle-based photoelectrodes under a) back- and b) front-side illumination. Transmittance is calculated using Beer-Lambert's law and is below 2% error compared to the measured transmittance in the spectral range of 400nm to 590nm (2.1eV, band gap of LTON). The experimental variation is obtained by measuring four different LTON photoelectrodes.

DFT calculations

DFT computational details - Our DFT calculations were performed with a kinetic energy cutoff of 40 Ry for the wavefunctions and a cutoff of 320 Ry for the augmented density. Electron-core interactions are described by ultrasoft

pseudopotentials with La(5s, 5p, 5d, 6s, 6p), Ti(3s, 3d, 3p, 4s), O(2s, 2p) and N(2s, 2p) valence electrons, where the O and N potentials were combined into a virtual crystal potential at $2/3$ and $1/3$ weight respectively, describing a complete disorder on the anion site. For the 20-atom orthorhombic cell, reciprocal space was sampled using a 6x4x6 mesh. Atoms were relaxed until forces converged below 0.05 eV/Å. Due to a code limitation, the dielectric constant was computed using DFPT without inclusion of the Hubbard U correction.

Electronic band structure - In Fig. S14, we show the band structure of orthorhombic LTON within the virtual crystal approximation to describe disorder on the anion site. Within this description, the material exhibits a direct bandgap of 1.96 eV at the Γ -point of the Brillouin zone which agrees reasonably well - given the use of a semilocal functional - with the experimentally measured 2.1eV² but is larger than calculations using explicit disorder models on the anion site¹⁰.

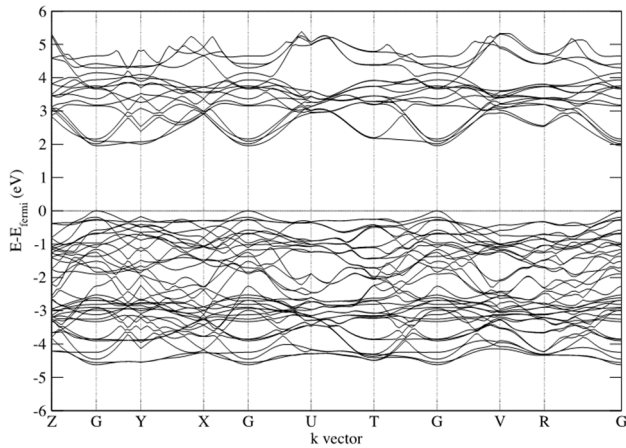


Fig. S14. Electronic band structure of orthorhombic LaTiO₂N along high-symmetry lines of the Brillouin zone.

Full dielectric tensor - Considering both electronic and ionic contributions, we obtain the following dielectric permittivity tensor for orthorhombic LaTiO₂N:

$$\begin{pmatrix} 19.458105 & 0.057050 & -0.466666 \\ 0.057050 & 11.451939 & -0.632479 \\ -0.466666 & -0.632479 & 13.897091 \end{pmatrix}$$

Semiconductor physics simulation

Computational details for charge transport and conservation - Convergence was obtained with a direct MUMPS solver fully coupled for the corresponding variables, i.e. electron and hole concentrations and electric potential. A relative tolerance in the hole and electron concentrations and the electric potential of 10^{-3} was used as a convergence criterion. For the 2D model, the mesh convergence was obtained for mesh element number, $n_{\text{mesh}} = d/5$ nm along the height and width with symmetric mesh distributions and an element ratio of 15. The symmetric distribution ensured a highly resolved mesh at each boundary in the model.

I-V curves for varying light intensity - Numerical and experimental photocurrent-voltage curves of best-LTON photoelectrode under back-side illumination for varying light intensities are depicted Fig. S15.

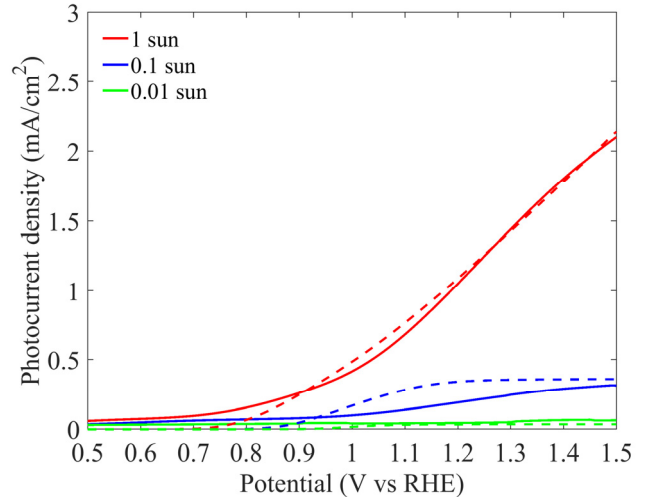


Fig. S15. Numerical (dashed lines) and experimental (solid lines) photocurrent-voltage curves of best-LTON photoelectrode under back-side illumination for varying light intensities (1, 0.1, and 0.01 sun).

Photoelectrode with the entire thickness being active - I-V curves of LTON particle-based PE with the entire thickness of the photoelectrode being active, i.e. without any potential loss along the thickness of the PEs, are depicted in Fig. S16.

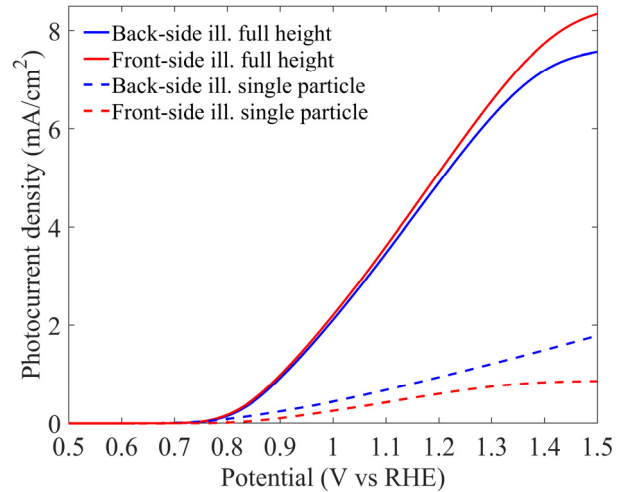


Fig. S16. Numerical and experimental photocurrent-voltage curves of best-LTON PEs with entire thickness (8.43µm) being active and only the first single particle's layer (1.42µm) being active under back- and front-side illumination. Thus, there is no potential loss along the thickness of the PE.

Electron mobility - The impact of electron mobility on the photocurrent under back- and front-side illumination is depicted in Fig. S17. There is no effect of electron mobility on the photocurrent under back-side illumination. Under front-side illumination, the photocurrent is also independent of the electron mobility although below a mobility of $0.1\text{cm}^2\text{V}^{-1}\text{s}^{-1}$, there is suddenly no photocurrent. The electron transport is only relevant to maintain charge conservation to have holes leaving the semiconductor to make the oxygen evolution reaction. Nevertheless, the charge conservation cannot be maintained if the mobility of electron becomes too small. Then, the electron cannot be collected anymore and will recombine with holes leading to the loss of the photocurrent as depicted in Fig. S17.

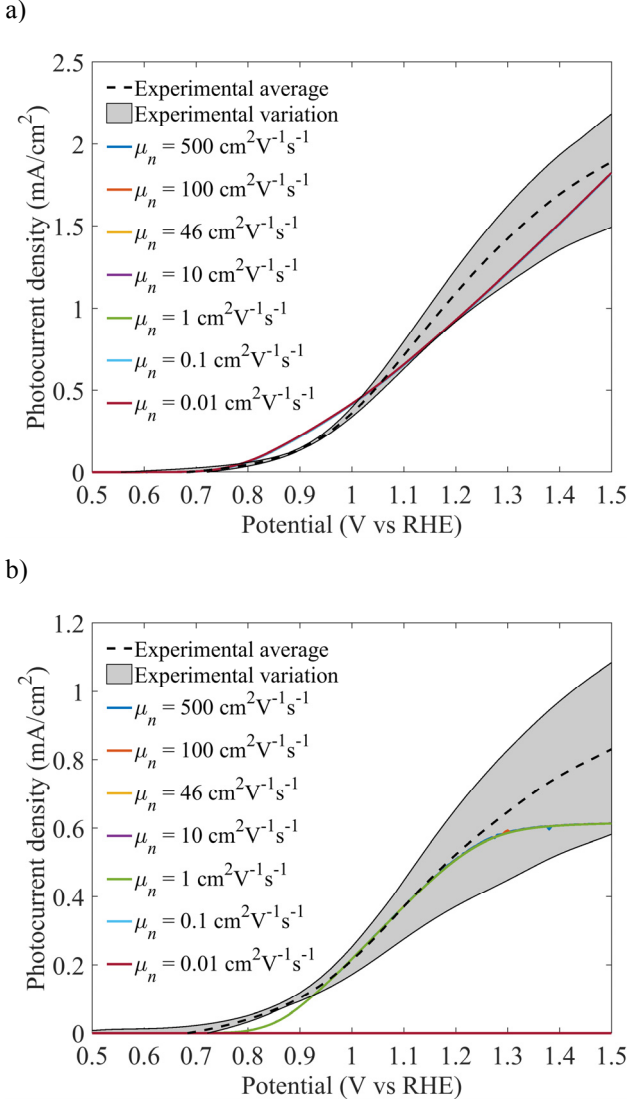


Fig. S17. Numerical and experimental photocurrent-voltage curves of best-LTON PEs under a) back- and b) front-side illumination for varying electron mobilities.

Doping concentration - The impact of doping concentration on the calculated photocurrents under back- and front-side illumination is depicted in Fig. S18, together with the experimentally measured ones. The doping concentration has a variety of opposing effects on the performance. First, increasing the doping concentration increases the electron density of the particle in the bulk ($n \approx N_D^+$) but also in the SCL, which increases the recombination rate and thus decreases the photocurrent. Second, the SCL is thinned, reducing the drift current. On the other hand, since the SCL is reduced, the electric field (gradient of the potential) is locally increased, providing a stronger charge separation force.

Under back-side illumination, it appeared that a change in the doping concentration did not affect the photocurrent (Fig. S18.a). We conclude that the doping concentration and the recombination rate related to the change in the doping concentration are not limiting under back-side illumination. Indeed, both electron and hole paths are short under back-side illumination and the good transport and recombination properties of LTON prevent charges to recombine. In contrast, the photocurrent under front-side was more affected by the doping concentration because the electron transport followed a longer path in which recombination and doping concentration started to play a role (Fig. S18.b). Nevertheless, the doping concentration did not appear as a key parameter for the

photocurrent. Indeed, the photocurrent density is only slightly reduced from 0.59 mA/cm² to 0.50 mA/cm² at 1.23 V vs RHE when reducing the doping concentration from 10¹⁶cm⁻³ to 10¹⁹cm⁻³. Thus, a large range of doping concentration (from 1·10¹⁶cm⁻³ to 1·10¹⁸cm⁻³) satisfied the calculated photocurrents within experimental variation.

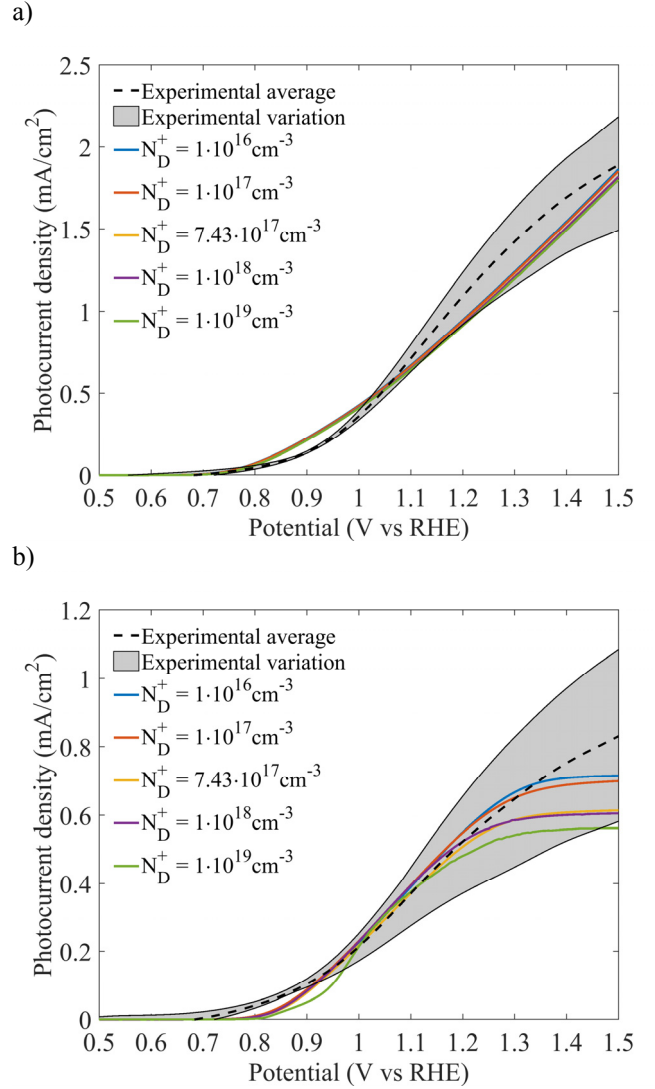


Fig. S18. Numerical photocurrent-voltage curves of best-LTON PEs under a) back- and b) front-side illumination for varying doping concentration.

Numerical I-V curves for bare-LTON - The numerical I-V curves for bare-LTON is presented in Fig. S19. The numerical photocurrent is well inside the experimental error bars for potential above 1.2 V vs RHE but the numerical onset potential is higher than the experimental one. The effective lifetimes of electron and holes are 0.01 ns and the interfacial hole velocity is 8.2·10⁻⁹cm/s. This experimental photocurrent in the potential range of 0.6 V to 1 V vs RHE can be attributed to a photocorrosion current present in LTON. It might also be attributed to a transient current attributed to high transient effects in this potential region³.

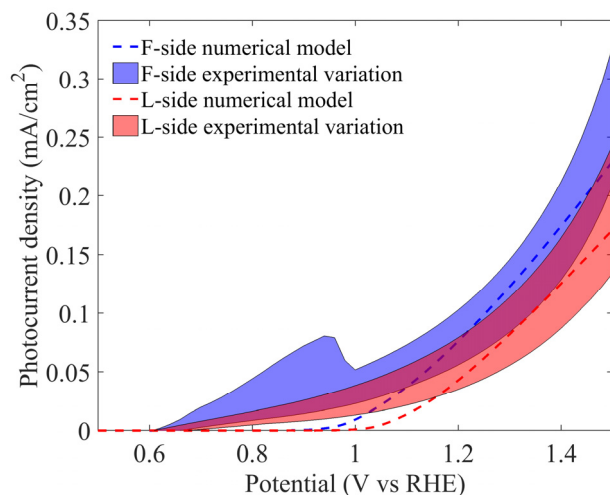


Fig. S19. Numerical and experimental photocurrent-voltage curves of bare-LTON under back- and front-side illumination.

References

- 1 S. Suter, M. Cantoni, S. Pokrant and S. Haussener, *Linking Morphology and Multi-Physical Transport in Structured Photoelectrodes*, Manuscript in preparation, 2018.
- 2 A. Kasahara, K. Nukumizu, G. Hitoki, T. Takata, J. N. Kondo, M. Hara, H. Kobayashi and K. Domen, *J. Phys. Chem. A*, 2002, **106**, 6750–6753.
- 3 S. Landsmann, A. E. Maegli, M. Trottmann, C. Battaglia, A. Weidenkaff and S. Pokrant, *ChemSusChem*, 2015, **8**, 3451–3458.
- 4 T. Hisatomi, T. Minegishi and K. Domen, *Chem. Soc. Japan*, 2012, **655**, 647–655.
- 5 T. Minegishi, N. Nishimura, J. Kubota and K. Domen, *Chem. Sci.*, 2013, **4**, 1120.
- 6 C. Le Paven-Thivet, A. Ishikawa, A. Ziani, L. Le Gendre, M. Yoshida, J. Kubota, F. Tessier and K. Domen, *J. Phys. Chem. C*, 2009, **113**, 6156–6162.
- 7 S. Dilger, S. Landsmann, M. Trottmann and S. Pokrant, *J. Mater. Chem. A*, 2016, **4**, 17087–17095.
- 8 N. Nishimura, B. Raphael, K. Maeda, L. Le Gendre, R. Abe, J. Kubota and K. Domen, *Thin Solid Films*, 2010, **518**, 5855–5859.
- 9 P. E. Ciddor, *Appl. Opt.*, 1996, **35**, 1566–1573.
- 10 S. Ninova and U. Aschauer, *J. Mater. Chem. A*, 2017, **00**, 1–7.